Quantifying Exhumation at the Giant Pulang Porphyry Cu-Au Deposit Using U-Pb-He Dating

Cheng-Biao Leng,[1,†] David R. Cooke,[2] Zeng-Qian Hou,[3] Noreen J. Evans,[4] Xing-Chun Zhang,[1] Wei T. Chen,[1] Martin Danišík,[4] Brent I.A. McInnes,[4] and Jie-Hua Yang[1]

[1]*State Key Laboratory of Ore Deposit Geochemistry, Institute of Geochemistry, Chinese Academy of Sciences, Guiyang 550081, China*

[2]*Center for Ore Deposits and Earth Sciences (CODES), University of Tasmania, Hobart, Tasmania 7001, Australia*

[3]*Institute of Geology, Chinese Academy of Geological Sciences, Beijing 100037, China*

[4]*John de Laeter Centre/Applied Geology, The Institute for Geoscience Research (TIGeR), Curtin University, Bentley, Western Australia 6845, Australia*

Abstract

The Triassic Pulang porphyry Cu-Au deposit, located in the South Yidun terrane, is the oldest and one of the largest porphyry deposits in the southeastern Tibetan Plateau. The mineralization occurs mostly in the potassic alteration zone of the Pulang intrusive complex. U-Pb-He triple dating, namely apatite (U-Th)/He, zircon U-Pb, and zircon (U-Th)/He dating, together with inverse thermal modeling, reveals that the Pulang complex was emplaced at a paleodepth of ~5.0 to 6.5 km at 215 ± 2 Ma. The deep-level emplacement of the complex, coupled with the episodic replenishment of the magma chamber, gave rise to the establishment of a prolonged magmatic-hydrothermal system at Pulang.

Although a range of single-grain zircon and apatite (U-Th)/He ages were obtained on each sample, the weighted mean zircon and apatite (U-Th)/He ages vary systematically with elevation, defining a multistage cooling/denudation history at Pulang. Specifically, three phases of cooling were recognized from inverse thermal modeling, including rapid cooling (80°–120°C/m.y.) in the Late Triassic, moderate cooling (3°–5°C/m.y.) from the Late Triassic to Early Cretaceous, and a protracted slow cooling period (<1°C/m.y.) from the Early Cretaceous to the present day. The first phase of cooling can be mainly attributed to magmatic cooling, whereas the later two phases of cooling were predominantly controlled by uplift and denudation processes. Moreover, the remarkable decrease in the cooling rate from the second to the third phase can be linked to a decreasing erosion rate during the third phase, supported by age-elevation relationships. Overall, our results indicate that the Pulang complex experienced two stages of exhumation at 33 to 45 m/m.y. and 5 to 17 m/m.y. Based on these data, we estimate that approximately 558- to 1,099-m thickness of materials have been removed from the Pulang complex during uplift and erosion, including a large volume of ore.

The long time span (>50 m.y.) of extremely slow cooling and erosion at Pulang could be related to the formation and preservation of a peneplain on the southeastern Tibetan Plateau since the Late Cretaceous. A relict peneplain thus signifies a favorable tectonic environment for the preservation of ancient porphyry systems worldwide.

Introduction

Porphyry ore deposits are products of complex magmatic and hydrothermal activity at convergent plate margins (Richards, 2011; Cooke et al., 2014) and commonly form at paleodepths of 1 to 6 km (mode average of ~2 km; Wilkinson and Kesler, 2007; Yanites and Kesler, 2015). Previous compilations of geochronological data revealed that porphyry deposits worldwide typically have Phanerozoic ages, with a particularly strong Cenozoic age population (e.g., Singer et al., 2008). This temporal distribution of porphyry deposits largely reflects the increased likelihood of older deposits having been destroyed by continuous erosion. Quantifying postmineralization exhumation processes has thus become fundamental to understanding how and when hypogene ores were unroofed after formation and when they were exposed at the paleosurface. In addition, the exhumation history of porphyries can provide insight into regional, and even global, tectonic evolution (e.g., Yanites and Kesler, 2015; Zhao

et al., 2016). Our understanding of the timing of emplacement and exhumation processes has been facilitated by the emergence of low-temperature thermochronometry methods (e.g., Wolf et al., 1996; Farley et al., 1998).

Fission-track and (U-Th)/He dating are two common thermochronological methods. They have closure temperatures (T_c) ranging from ~60° to 250°C and are thus sensitive to exhumation through crustal depths of one to several kilometers (e.g., Reiners and Brandon, 2006). The apatite (U-Th)/He system has the lowest closure temperature (45°–70°C; Farley et al., 1998; Wolf et al., 1998) and has the potential to place temporal constraints on exhumation processes from 1- to 3-km depth to the surface under a geothermal gradient of 20° to 40°C/km, commensurate with the average depth of most porphyry systems. The apatite (U-Th)/He thermochronometer has been used widely in combination with other thermochronometers to quantify the cooling and exhumation processes at porphyry and/or skarn deposits (e.g., McInnes et al., 1999, 2005a, b; Masterman et al., 2005; Xu et al., 2006; Harris et al., 2008; Bineli Betsi et al., 2012; Braxton et al., 2012; Zhao et

al., 2015, 2016), orogenic-type Au deposits (Zeng et al., 2013; Liu et al., 2017), and diamondiferous kimberlite occurrences (e.g., McInnes et al., 2009; Evans et al., 2013). McInnes et al. (2005a, b) performed apatite (U-Th)/He, zircon (U-Th)/He, and zircon U-Pb dating on samples from porphyry deposits in Iran, Chile, and Indonesia. Combined with inverse numerical modeling (i.e., 4DTherm; Fu et al., 2010), the data were used to decode thermal histories (magmatic through hydrothermal and exhumation) over a 700°C temperature interval. However, modeling requires knowledge and assumptions of physicochemical parameters of the igneous bodies and their country rocks (e.g., geothermal gradient, size of intrusion, temperature, etc.), which are not always available. The vertical transect method, devised by Wagner and Reimer (1972), has been utilized to deduce simple age-elevation relationships for thermochronometers. This relationship provides a direct basis to estimate long-term erosion rate, independent of geothermal gradient and other parameters, and has been used extensively in the study of geomorphic evolution (e.g., Reiners et al., 2003; Flowers and Farley, 2012).

We have applied the vertical transect sampling strategy, U-Pb-He dating, and numerical modeling to study the cooling and erosion history of the giant Pulang porphyry Cu-Au deposit, which formed during the Late Triassic in the Yidun terrane, at the southeastern margin of the Tibetan Plateau. Pulang was selected for the case study, because it is the oldest and one of the largest porphyry deposits in southeastern Tibet, and several >1,000-m deep drill holes provide excellent vertical transects for sampling. In addition to quantifying the thermal history of the deposit and determining the uplift and erosion rate at Pulang, the research aims to shed light on the tectonic evolution of the southeastern Tibetan Plateau and the preservation of ancient porphyry deposits.

Geologic Background

Geology of the Yidun terrane

The Yidun terrane, also known as the Chuanxi Plateau or Litang Plateau, is located between the Qiangtang and Songpan-Ganzi terranes (Fig. 1a). It is characterized by abundant low-relief surfaces (i.e., relict peneplains) at high elevations (Clark et al., 2005; Tian et al., 2014). The basement of the Yidun terrane is composed of Neoproterozoic granitic gneisses and metavolcanic rocks, which are similar to the lithological assemblages of the Kangding complex in the western margin of the Yangtze block (Fig. 1b), implying that the Yidun terrane was part of the Yangtze block prior to the Early Permian (Chang, 2000; Song et al., 2004). Triassic sequences of clastic rocks, intercalated with arc-type volcanic rocks, overlie Paleozoic sequences (Fig. 1b). These volcanic rocks formed during the westward subduction of the Ganzi-Litang Ocean in the Late Triassic (e.g., Leng et al., 2014). A number of large coeval granite batholiths, and felsic-intermediate porphyry stocks and dikes with associated ore deposits, were emplaced into the upper crust of the Yidun terrane (Reid et al., 2007; Leng et al., 2014; Tian et al., 2014). The absence of Jurassic-Cretaceous strata indicates that this terrane was uplifted above sea level no later than the Early Jurassic.

The Yidun terrane experienced at least two main phases of deformation and metamorphism from Early Triassic to Early Jurassic (Reid et al., 2005; Roger et al., 2011). The early phase of deformation and metamorphism was recorded mainly by Paleozoic sequences in the western Yidun terrane, producing up to amphibolite facies metamorphic rocks. This phase of deformation and metamorphism resulted from northeastward accretion of the eastern Qiangtang terrane onto the Yidun terrane along the southern Jinsha suture zone in the Early Triassic (Reid et al., 2005). Late-phase metamorphic grades were up to greenschist facies and affected Middle-Late Triassic rocks of the eastern Yidun terrane during the Late Triassic to Early Jurassic (Reid et al., 2005; Yang et al., 2012). This stage of metamorphism and deformation was related to the closure of the Ganzi-Litang Ocean and the subsequent collision between the Songpan-Ganzi and Yidun terranes (Reid et al., 2005; Yang et al., 2012).

The Yidun terrane was intruded by the Mesozoic-Cenozoic granitoids that were derived from melting of old continental crust in an intraplate extensional setting (Reid et al., 2007; Wang et al., 2014). However, the emplacement of these Cretaceous felsic plutons did not affect the cooling history of the Triassic plutons (e.g., Reid et al., 2005; Roger et al., 2011). Following collision of the Indian and the Eurasian plates in the Tertiary, the Yidun terrane was incorporated into the modern Tibetan Plateau and deformed by numerous strike-slip fault movements (Wang and Burchfiel, 2000; Zhang et al., 2015, 2017).

Geology and previous geochronology of the Pulang deposit

The Pulang porphyry deposit, located in the south Yidun terrane, contains proven reserves of approximately 4.31 million tonnes (Mt) of Cu and 113 t of Au, with an average grade of 0.34% and 0.09 g/t, respectively (Li et al., 2011). Detailed geologic descriptions have been provided by Fan and Li (2006) and Li et al. (2011), with a summary presented below.

The Cu-Au orebody is mostly confined within the Pulang intrusive complex, which was emplaced into the Triassic clastic and volcanic rocks of the Tumugou Formation (Fig. 2a). The complex is composed of five phases of porphyry stocks and dikes and covers an area of 16 km². The stocks include premineralization quartz diorite porphyry, synmineralization monzodiorite porphyry and quartz monzonite porphyry stocks, and postmineralization granodiorite porphyry and andesite porphyry dikes. Associated hydrothermal alteration assemblages include potassic, sericite, and propylitic alterations, which were extensively developed in the Pulang complex. Potassic alteration generally occupies a central zone, which is surrounded by propylitic alteration on the periphery. Both alteration types were locally overprinted by late sericite alteration. Ores occur mainly within the potassic alteration zone (Fig. 2a, b). Biotite-magnetite alteration affected adjacent clastic rocks of the Tumugou Formation and produced hornfels zones surrounding the complex (Fig. 2a).

During the past decade, many attempts have been made to date the Pulang complex and ores (Table 1). Wang (2008) obtained zircon SHRIMP U-Pb ages of 228 to 226 Ma for the quartz monzonite porphyry, slightly older than the zircon isotope dilution-thermal ionization mass spectrometry (ID-TIMS) U-Pb age of 211.8 ± 0.5 Ma for the same porphyry (Pang et al., 2009). Pang et al. (2009) also obtained two zircon U-Pb ages of 221.0 ± 1.0 and 206.3 ± 0.7 Ma for the
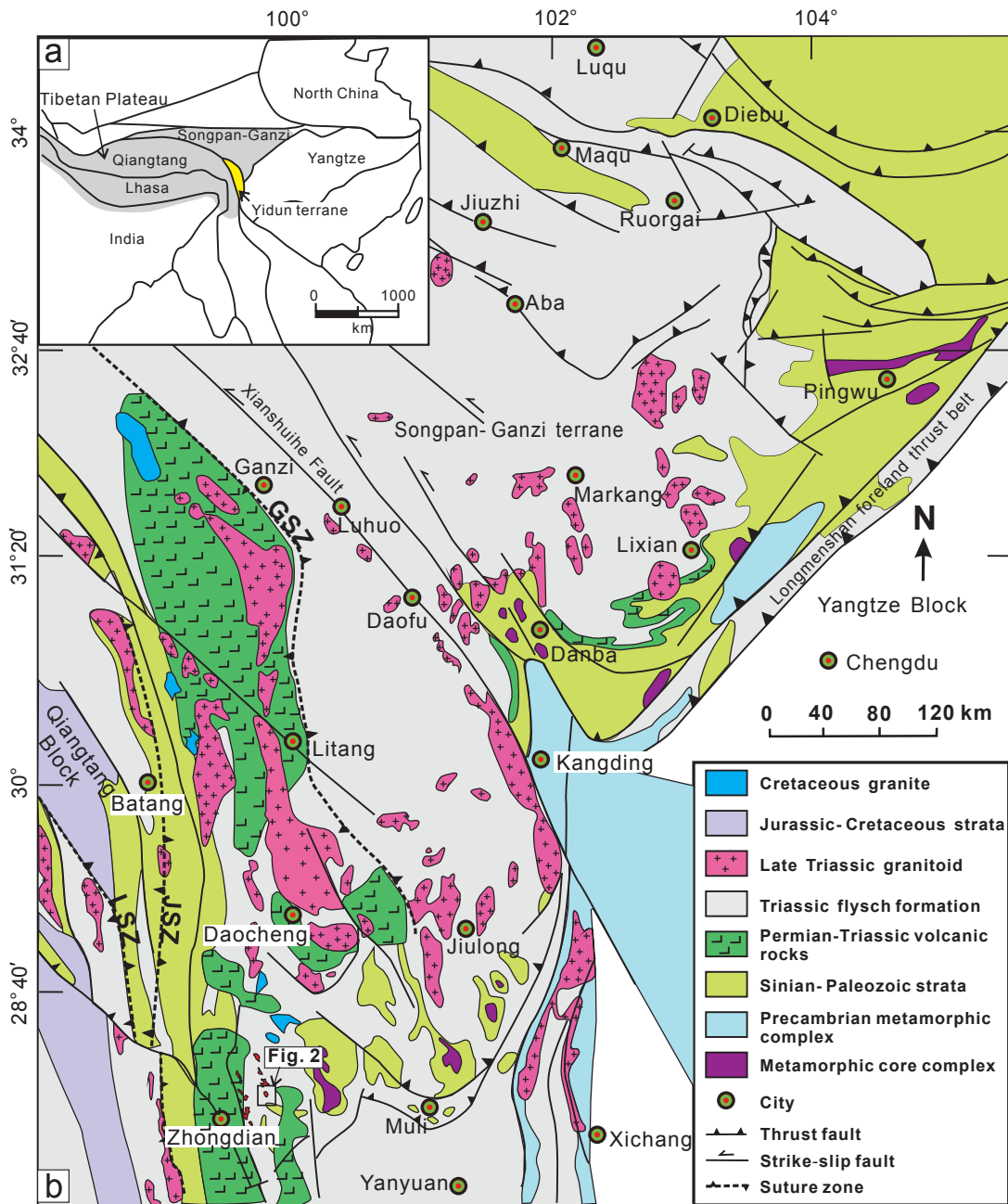
Fig. 1. (a) Tectonic framework of the Tibetan Plateau, highlighting location of the study area (modified from Reid et al., 2005). (b) Geologic map of the Yidun terrane and its adjacent areas (modified from Yan et al., 2008). Abbreviations: GSZ = Ganzi-Litang suture zone, JSZ = Jinsha suture zone, LSZ = Lancangjiang suture zone.

quartz diorite porphyry and granodiorite porphyry, respectively. Similar but less precise U-Pb ages for these porphyries were also provided by Wang et al. (2011) and Liu et al. (2013). Zeng et al. (2006) dated the mineralization, providing a reliable Re-Os age of 213 ± 3.8 Ma for molybdenite. The hornblende and biotite grains separated from some potassic altered porphyries yielded $^{40}Ar/^{39}Ar$ plateau ages varying from 216 to 210 Ma (Zeng et al., 2006; Wang, 2008; Li et al., 2011), broadly comparable to the molybdenite Re-Os ages and thus probably recording the timing of ore-related potassic alteration. In contrast, two K-feldspar samples separated from the

quartz monzonite porphyry yielded much younger K-Ar and $^{40}Ar/^{39}Ar$ plateau ages of ~182 Ma (Zeng et al., 2006; Wang, 2008; Li et al., 2011). Considering that the closure temperature of the K-feldspar Ar-Ar system is as low as ~150° to 350°C (e.g., Foland, 1994; Villa and Hanchar, 2013), these ages likely represent a late thermal event.

Sampling and Analytical Methods

Given that an age vs. elevation profile can be used to estimate exhumation rate independently, we collected seven porphyry samples at approximately 500-m intervals from some
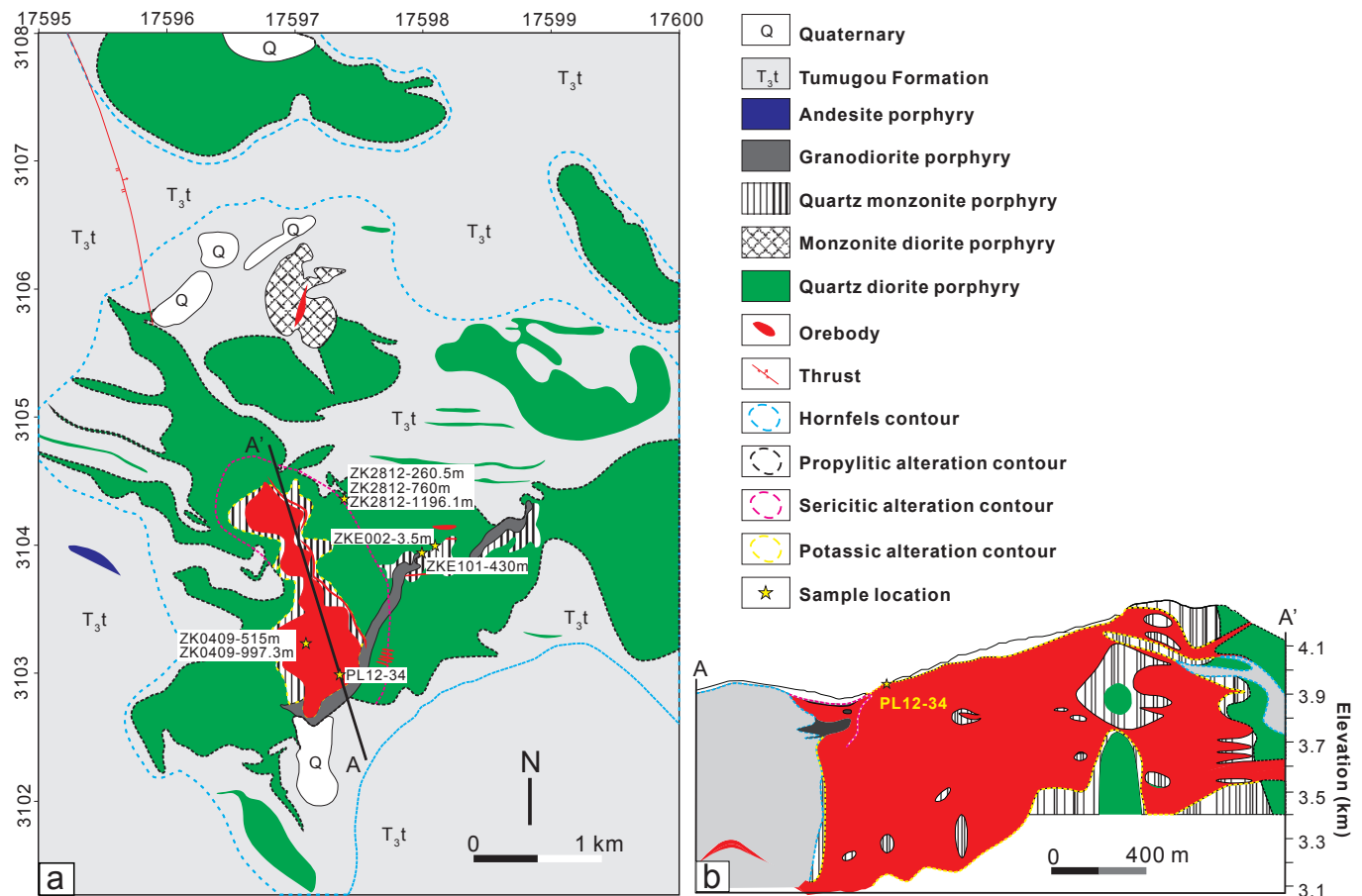
Fig. 2. (a) Simplified geologic map of the Pulang porphyry Cu-Au deposit (modified from Li et al., 2011), highlighting sample locations. (b) Geologic cross section A–A'.

Table 1. Summary of Geochronological Data for the Pulang Deposit

Mineral	Dating method	Age (Ma, 2σ)	Host rock	Reference
Zircon	ID-TIMS	206.3 ± 0.7	GP	Pang et al., 2009
Zircon	ID-TIMS	211.8 ± 0.5	QMP	Pang et al., 2009
Zircon	ID-TIMS	221.0 ± 1.0	QDP	Pang et al., 2009
Zircon	SHRIMP U-Pb	226 ± 3.0	QMP	Wang et al., 2008
Zircon	SHRIMP U-Pb	226.3 ± 2.8	QMP	Wang et al., 2008
Zircon	SHRIMP U-Pb	228 ± 3.0	QMP	Wang et al., 2008
Zircon	LA-ICP-MS U-Pb	224.2 ± 1.7	QDP	Wang et al., 2011
Zircon	LA-ICP-MS U-Pb	217.9 ± 1.8	QDP	Wang et al., 2011
Zircon	LA-ICP-MS U-Pb	219.6 ± 3.5	QDP	Liu et al., 2013
Zircon	LA-ICP-MS U-Pb	212.8 ± 1.9	QMP	Liu et al., 2013
Molybdenite	Re-Os	213 ± 3.8	Qtz-Moly veinlet in QMP	Zeng et al., 2006; Li et al., 2011
Biotite	K-Ar	221.5 ± 2.0	QDP	Zeng et al., 2006; Li et al., 2011
Biotite	K-Ar	230.9 ± 2.2	QMP	Zeng et al., 2006; Li et al., 2011
Biotite	K-Ar	223.5 ± 2.1	QMP	Zeng et al., 2006; Li et al., 2011
Biotite	K-Ar	235.4 ± 2.4	QMP	Zeng et al., 2006; Li et al., 2011
Hornblende	^{40}Ar/^{39}Ar	212.7 ± 2.9	QDP	Wang, 2008
Hornblende	^{40}Ar/^{39}Ar	212.1	QDP	Li et al., 2009
Hornblende	^{40}Ar/^{39}Ar	209.4 ± 1.7	GP	Li et al., 2009
Biotite	^{40}Ar/^{39}Ar	216.0 ± 1	QMP	Zeng et al., 2006; Li et al., 2011
Biotite	^{40}Ar/^{39}Ar	214.6 ± 0.9	QMP	Zeng et al., 2006; Li et al., 2011
Biotite	^{40}Ar/^{39}Ar	212.3 ± 1.4	QMP	Li et al., 2009
Biotite	^{40}Ar/^{39}Ar	210.3 ± 0.8	QMP	Wang, 2008
K-feldspar	^{40}Ar/^{39}Ar	181.7 ± 9.3	QMP	Wang, 2008
K-feldspar	K-Ar	182.5 ± 1.8	QMP	Zeng et al., 2006; Li et al., 2011

Note: All the ^{40}Ar/^{39}Ar dates are reported as plateau ages for the K-bearing minerals in this paper, unless otherwise specified
Abbreviations: GP = granodiorite porphyry, ID-TIMS = isotope dilution-thermal ionization mass spectrometry, LA-ICP-MS = laser ablation-inductively coupled plasma-mass spectrometry, Moly = molybdenite, QDP = quartz diorite porphyry, QMP = quartz monzonite porphyry, Qtz = quartz

representative deep drill holes (e.g., ZK0409 and ZK2812) and one sample from a surface outcrop (Table 2; Fig. 2). Zircon and apatite crystals were separated from crushed rock using a combination of magnetic and heavy liquid separation techniques. Individual crystals were handpicked under a binocular microscope. Zircon and apatite crystals were used for zircon U-Pb and zircon and apatite (U-Th)/He dating. Detailed dating results are provided in Electronic Appendix Table A1. Table 2 gives an overview of sampling locations, lithology, and multiple radiometric ages for the samples.

Zircon LA-ICP-MS U-Pb dating

Zircon U-Pb dating was performed on an Agilent 7500cs quadrupole inductively coupled plasma-mass spectrometer (ICP-MS) with a 193-nm Coherent Ar-F gas laser at the University of Tasmania, Hobart, Australia. Downhole fractionation, instrument drift, and mass bias correction factors for Pb/U ratios were calculated using standard blocks, including two analyses of the primary standard 91500 (Wiedenbeck et al., 1995) and one analysis on each of the secondary standard zircons (Temora, Black et al., 2003; and GJ-1, Jackson et al., 2004), which were analyzed at the beginning of the session and every 15 unknown zircons, using the same spot size and analytical conditions as those used on the samples. Additional secondary standards, Plešovice and Mud Tank, were also analyzed to monitor the analytical accuracy. The correction factor for the $^{207}Pb/^{206}Pb$ ratio was calculated using large spots of NIST610 analyzed every 30 unknowns and corrected using the values recommended by Baker et al. (2004).

Each analysis began with a 30-s blank gas measurement followed by a further 30 s of analysis with the laser firing. Zircons were sampled using 32-µm spots using a frequency of 5 Hz and an energy density (measured at the sample surface) of approximately 2 J/cm². A flow of He carrier gas at a rate of 0.35 L/min carried ablated material out of the chamber to be mixed with Ar gas and carried to the ICP-MS plasma torch. Isotopes measured were ^{49}Ti, ^{56}Fe, ^{90}Zr, ^{178}Hf, ^{202}Hg, ^{204}Pb, ^{206}Pb, ^{207}Pb, ^{208}Pb, ^{232}Th, and ^{238}U, with each element measured every 0.16 s with longer counting times on the Pb isotopes compared to the other elements. Data were reduced using methods described in Meffre et al. (2008) and Sack et al. (2011). Element abundances on zircons were calculated using Zr as the internal standard element, assuming stoichiometric proportions (43.14% Zr in zircon) and using NIST610 to correct for mass bias and drift. Secondary standards reproduced

accepted values within 2%. Analytical results for the standards are presented in Electronic Appendix Table A2.

Zircon and apatite (U-Th)/He dating

Zircon and apatite (U-Th)/He dating was conducted at the John de Laeter Centre, Curtin University, Western Australia, using methods detailed in Evans et al. (2005, 2013). Zircon and apatite grains were selected by handpicking to avoid grains with cracks or U- and Th-rich mineral inclusions that may contribute excess He to the analysis. Grain measurements were taken for the calculation of an alpha correction factor (Ft; Farley, 2000). Helium was thermally extracted from single crystals of zircon or apatite, loaded into niobium or platinum microcrucibles (respectively), and heated using a diode laser. ^{4}He abundances were determined by isotope dilution using a pure ^{3}He spike, calibrated daily against an independent ^{4}He standard. The uncertainty in the ^{4}He measurement of sample was <1%. For zircon, the U and Th concentrations were determined using isotope dilution-inductively coupled plasma-mass spectrometry. Zircon grains were removed from the laser chamber and transferred to Parr bombs, where they were spiked with ^{235}U and ^{230}Th and digested at 240°C for 40 h in HF. Standard solutions containing the same spike amounts as samples were treated identically, as were a series of unspiked reagent blanks. A second bombing in HCl for 24 h at 200°C ensured dissolution of fluoride salts, and final solutions were diluted to 10% acidity for analysis on an Agilent 7500cs mass spectrometer. For degassed apatite, the U and Th contents were determined by isotope dilution using ^{235}U and ^{230}Th spikes. Twenty-five µL of a 50% HNO_3 solution containing ~15 ppb of ^{235}U and 5 ppb of ^{230}Th was added to each sample. The apatite was digested in the spiked acid for at least 12 h to allow the spike and sample isotopes to equilibrate. Standard solutions containing the same spike amounts as the samples, in addition to 25 µL of a standard solution containing 27.6 ppb U and 28.4 ppb Th, were treated identically, as were a series of unspiked reagent blanks. Prior to analysis on the mass spectrometer, 250 µL of MilliQ water was added.

Both U and Th isotope ratios were measured to a precision of <2%. The (U-Th)/He thermochronology method at Curtin University has an overall precision of <6% for zircon (based on repeated analysis of an in-house standard) and 2.5% for apatite based on multiple age determinations (n = 70) of Durango standard, which produce an average age of 31.5 ±

Table 2. Summary of Locations, Lithology, and Dating Results for the Pulang Complex Samples

Sample	Location	Elevation	Lithology	Zircon U-Pb (Ma, 2σ)	ZHe[*] (Ma, 2σ)	AHe[*] (Ma, 2σ)
PL12-34	Surface, N28° 02.266'; E99° 59.401'	3,950 m	QMP	217.0 ± 1.3	142.3 ± 5.6	63.2 ± 2.4
PLZK0409-515m	Drill hole ZK0409, 515-m depth	3,497 m	QMP	216.4 ± 1.4	131.3 ± 5.1	54.5 ± 2.1
PLZK0409-997.3m	Drill hole ZK0409, 997.3 m depth	3,015 m	QMP	217.6 ± 1.3	119.7 ± 4.4	55.2 ± 2.5
PLZK2812-260.5m	Drill hole ZK2812, 260.5-m depth	4,009.5 m	QDP	215.2 ± 1.2		72.6 ± 3.8
PLZK2812-760m	Drill hole ZK2812, 760-m depth	3,510 m	QDP	215.2 ± 1.7	134.4 ± 7.2	72.4 ± 4.9
PLZK2812-1196.1m	Drill hole ZK2812, 1196.1-m depth	3,074 m	QDP	213.5 ± 1.9	110.3 ± 6.7	57.2 ± 2.9
PLZKE002-3.5m	Drill hole ZKE002, 3.5-m depth	4,225 m	QDP	218.1 ± 1.6	139.7 ± 7.6	105.8 ± 6.7
PLZKE101-430m	Drill hole ZKE101, 430-m depth	3,790 m	QDP	215.1 ± 1.7	133.5 ± 7.2	99.8 ± 5.2

Abbreviations: AHe = apatite (U-Th)/He, QDP = quartz diorite porphyry, QMP = quartz monzonite porphyry, ZHe = zircon (U-Th)/He
[*]Represents weighted mean age

1.6 (2σ) Ma (within error of the accepted age of 31.44 ± 0.18; McDowell et al., 2005).

Inverse thermal modeling

Numerical modeling techniques provide effective and complementary tools for interpreting real thermochronometry data. In this study, two computational modeling software programs (HeFTy and 4DTherm) were independently used to determine the thermal history of the Pulang complex, utilizing dating results determined in this work and previously published data. Here we provide a brief overview of the two approaches with detailed descriptions given in Ketcham (2005) and Fu et al. (2010), respectively.

HeFTy is one of the most popular thermal modeling programs for low-temperature thermochronological data, including apatite and zircon (U-Th)/He ages (Ehlers et al., 2005). In the latest version of this program (i.e., HeFTy v.1.9.3), the kinetic models of Flowers et al. (2009) and Guenthner et al. (2013) were used for apatite and zircon (U-Th)/He calculations, respectively. Input data for the inversions included apatite and zircon (U-Th)/He ages, grain dimensions, and U-Th concentrations. Models were constrained by the present-day surface temperature (i.e., 10 ± 2°C) and the time-temperature constraints placed around the published ⁴⁰Ar/³⁹Ar ages of hornblende and biotite (Table 1), and the zircon U-Pb ages of this study (Table 2). Models were run until 50 good fits, as defined in Ketcham (2005), were obtained.

4DTherm v.1.2 uses a 2-D explicit finite difference solution that addresses conduction cooling, magma convection, groundwater circulation, latent heat of crystallization, and fusion as well as exhumation and erosion processes (Ehlers et al., 2005; Fu et al., 2010). The main application of this program is to reconstruct cooling and exhumation histories of igneous intrusions, which is achieved by determining the emplacement depth of igneous intrusions and calculating the erosion rates for igneous rocks and corresponding country rocks (Ehlers et al., 2005). The calculation of erosion rates is mainly based on the input apatite and zircon (U-Th)/He data, whereas the emplacement depth and eroded thickness of the igneous body are determined through inverse modeling using an iterative trial-and-error strategy (see Fu et al., 2010). Data inputs to the program include the following: (1) size and shape of igneous and country rock units, (2) residual sizes, position, and properties of igneous bodies, (3) age data and closure temperatures, and (4) sample position. The outputs available after each successful run include digitized age-temperature cooling curves with highlighted key points and a number of physical parameters related to the dynamic processes of magmatic-hydrothermal cooling, such as depth and time of emplacement, cooling rates of different stages, exhumation/erosion rates for country and intrusion rocks, eroded thicknesses of intrusions, and the exposure time if the sample was exhumed to the surface (McInnes et al., 2005a; Fu et al., 2010).

Dating and Modeling Results

Zircon U-Pb ages

Most of the zircon grains from the Pulang complex are colorless and transparent, euhedral with clear concentric and oscillatory growth zoning in cathodoluminescence (CL) images. No inherited zircon or relict cores were observed in this study (Electronic App. Table A1). Three indistinguishable U-Pb ages (217.6 ± 1.3–216.4 ± 1.4 Ma) were obtained for the quartz monzonite porphyry samples collected at different sites of the complex (Table 2; Fig. 3a-c). Five quartz diorite porphyry samples also yielded similar zircon U-Pb ages, ranging from 218.1 ± 1.6 to 213.5 ± 1.9 Ma (Fig. 3d-h). These ages represent the maximum emplacement timing of the complex.

(U-Th)/He ages

In general, three to five single zircon and apatite grains were analyzed for each sample. The detailed results are given in Electronic Appendix Tables A3 and A4, and a summary with the weighted mean age for each sample is provided in Table 2. Overall, 32 single-grain zircon (U-Th)/He ages, varying from 167.1 ± 9 to 86.7 ± 4.7 Ma, were obtained from the samples. Notably, the age variations between single crystals from some samples (e.g., PLZK2812-1196.1m, PLZKE002-3.5m) exceed the analytical precision of <6%. In addition, 36 single-grain apatite (U-Th)/He ages, ranging from 156 ± 16.2 to 24.3 ± 0.9 Ma, were obtained. Similarly, there are also large intrasample age variations, which are beyond the analytical uncertainty of <2.5%. In order to avoid the potential influence of outliers on averaging dates of each sample, the Chauvenet criterion was utilized. This method has been used for outlier detection in previous studies (e.g., Fitzgerald et al., 2006; Liu et al., 2017). Consequently, seven single-grain zircon (U-Th)/He ages and nine single-grain apatite (U-Th)/He ages that failed the Chauvenet's criterion test were excluded from the determination of the mean and weighted mean ages (Electronic App. Tables A3, A4). Although the single-grain ages are relatively scattered, the weighted mean zircon and apatite (U-Th)/He ages generally display a positive correlation with elevation (Table 2; Fig. 4), allowing us to estimate long-term erosion rates of the Pulang complex. Using a least squares regression routine, we obtained two regression lines to fit the age-elevation data. The two lines predict two different exhumation processes, with an apparent erosion rate of 33.6 m/m.y. during the interval of 142 to 110 Ma and a rate of 15.3 m/m.y. from 106 to 54 Ma.

HeFTy modeling

Thermal history modeling results performed by HeFTy v.1.9.3 are plotted in Figure 5. Overall, the results reveal coherent time-temperature paths for all the analyzed samples. At least three phases of cooling were obtained based on the variable gradients of the weighted mean cooling paths: a phase of rapid cooling at a rate of ~80° to 120°C/m.y. in the Late Triassic, a period of slow cooling at a rate of ~3° to 5°C/m.y. from the Late Triassic to Early Cretaceous, and a phase of extremely slow and monotonic cooling at a rate of <1°C/m.y. from the Early Cretaceous to the present day. Additionally, as shown in Figure 5, all the analyzed samples experienced prolonged periods within the helium partial retention zones for both the zircon and apatite (U-Th)/He systems. Specifically, the residence time in the apatite helium partial retention zones was greater than 20 m.y., whereas the stay in the zircon helium partial retention zones lasted for ca. 10 to 20 m.y.
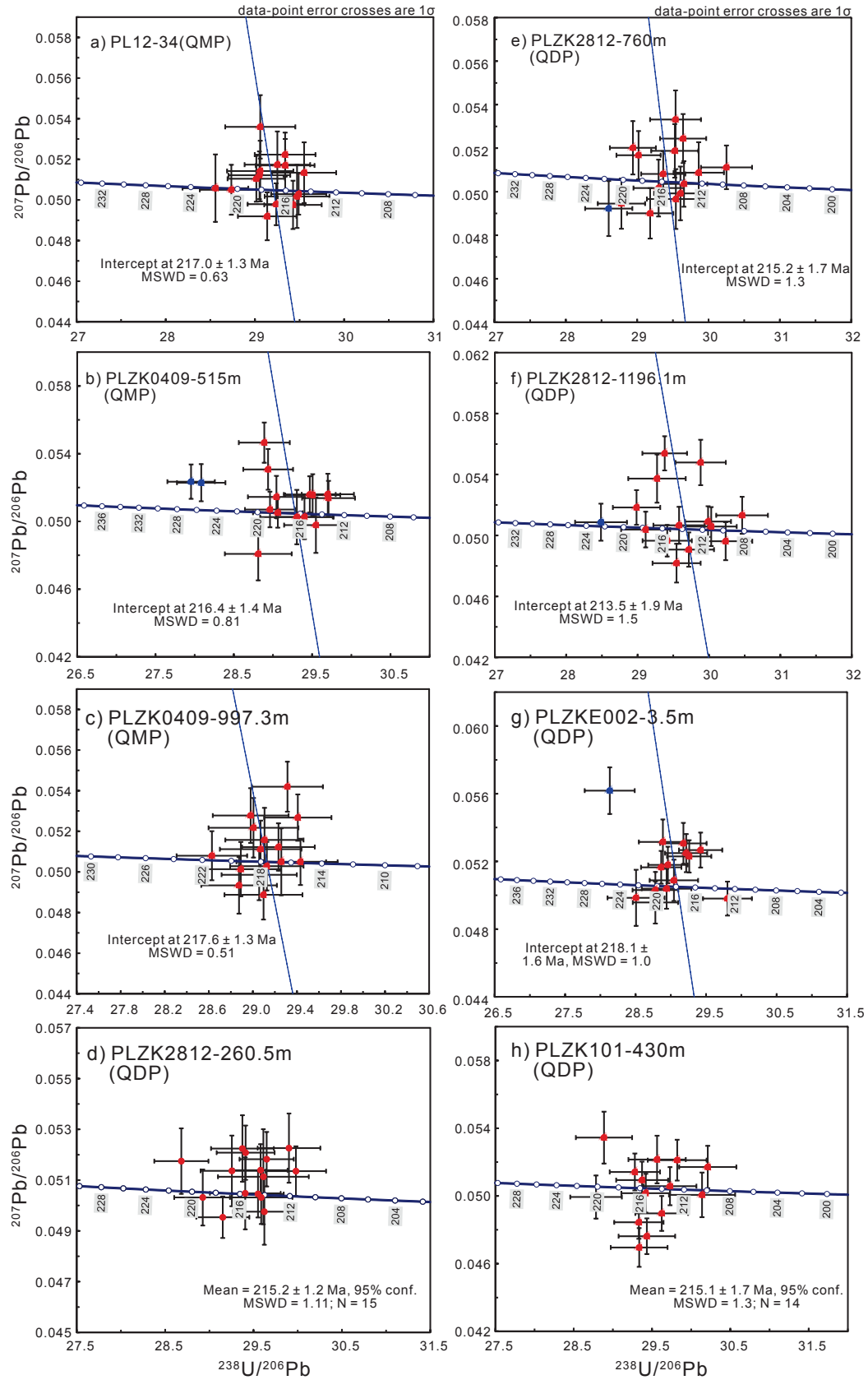
Fig. 3. Terra-Wasserburg plots of the zircon U-Pb data for the Pulang complex. The blue spots were excluded from age calculation. Abbreviations: MSWD = mean square of weighted deviates, QDP = quartz diorite porphyry, QMP = quartz monzonite porphyry.
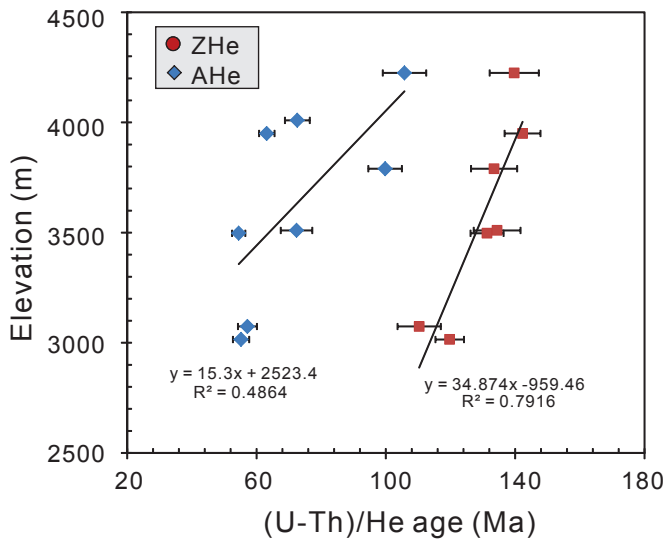
Fig. 4. Plot of elevation vs. (U-Th)/He ages for the Pulang complex. Abbreviations: AHe = apatite (U-Th)/He, ZHe = zircon (U-Th)/He.

4DTherm modeling

Based on geologic mapping and drill core logging at the Pulang deposit, the quartz monzonite porphyry was modeled as a 1.8- by 0.7-km oval cylindrical porphyry stock with a residual height of 3.0 km, while the quartz diorite porphyry was simplified as a 3.7- by 3.7-km cylindrical porphyry stock with a residual height of 4.5 km. The crystallization temperature of the zircon in the Pulang complex was estimated to be ~750°C by Wang (2008). The closure temperatures of zircon and apatite (U-Th)/He systems were calculated by the CLOSURE program of Brandon et al. (1998) at a cooling rate of 1°C/m.y. (see Electronic App. Tables A3, A4). The initial temperature of felsic magma at Pulang was assumed to be 800°C. Considering that the research area is sited in a tectonically active belt, the basal heat flow is set at 100 MW/M2, and the geothermal gradient of country rocks was set as 40°C/km. Other initial parameters are copied from the default values of the 4DTherm v.1.2 packages (see Fu et al., 2010, for details).

Four of the analyzed samples were successfully tested (Table 3; Fig. 6). The inferred emplacement depth of the Pulang complex is between 5.0 and 6.5 km, which is broadly consistent with the depth inferred from the Al-in-Hornblende barometer (84–215 MPa, Leng et al., 2018). Average cooling rates for the magmatic and exhumation stages were estimated as 112° to 140°C/m.y., and from 1.18° to 1.4°C/m.y., respectively. The duration of the 500° to 300°C interval was calculated as 0.56 to 1.58 m.y. for the quartz monzonite porphyry, which is consistent with the results obtained using hornblende and biotite ^{40}Ar/^{39}Ar plateau ages of Wang (2008) (see Table 1).

Moreover, 4DTherm estimated an exhumation/erosion rate of 2.2 to 16.8 m/m.y. for the Pulang complex, which is much lower than that of the country rock (32.7–45 m/m.y.). These rates are roughly commensurate with the values derived from the age-elevation relationships of the apatite and zircon (U-Th)/He data (see above). It is estimated that the Pulang complex was exposed to paleosurface at ~74.3 to 48.9 Ma, and the eroded thicknesses of the complex vary from 558 to 1,099 m.

Discussion

Evaluation of the thermochronological data

As mentioned above, the variation of (U-Th)/He ages within single grains—especially for apatite (U-Th)/He ages—exceeds relevant analytical error. It is thus essential to investigate potential factors causing the age dispersion. The factors may include variations in grain size, heterogeneous distribution of parental nuclides, implantation of He from neighboring U- and Th-rich minerals, presence of excess ^{4}He from fluid inclusions and/or undetected U- and Th-bearing particles, radiation damage that changed He retentivity and closure temperature, and cooling rate (e.g., Fitzgerald et al., 2006; Zhao et al., 2015; Danišík et al., 2017; Liu et al., 2017).

If the variable single-grain ages resulted from grain size differences, larger grains should have older ages. However, there is no positive correlation between equivalent spherical radius (R_{eq}) and (U-Th)/He ages, suggesting that grain size is not the dominant factor accounting for the intrasample dispersion in single-grain ages (Fig. 7a, b). The possibility of He implantation can also be ruled out, because no U- or Th-rich minerals were observed near zircon or apatite in thin section. A good linear correlation is seen between corrected He content and effective uranium (eU) concentration for both zircon and apatite (Fig. 7c, d), except for some outliers, arguing against the presence of excess ^{4}He. Although high radiation dosage of zircon could significantly increase He diffusion rates at low temperature (e.g., Reiners, 2005; Danišík et al., 2017), the relatively low U concentrations (mostly less than 500 ppm) as determined by laser ablation-inductively coupled plasma-mass spectrometry (LA-ICP-MS) analyses (Electronic App. Table A1) imply that the accumulated radiation damage is insufficient to cause the wide scatter of zircon (U-Th)/He ages (cf. Reiners, 2005; Zhao et al., 2015). Moreover, neither U nor Th zonation patterns were observed during the LA-ICP-MS analyses, suggesting that the heterogeneous distribution of parental nuclides is also not the dominant factor that resulted in the wide variation of single-grain ages at Pulang.

Therefore, the cooling rate seems the most likely factor responsible for dispersion of single-grain ages. As shown in Fitzgerald et al. (2006), if the cooling rate is less than 3°C/m.y., the variation in single-grain ages is much greater than it would be at higher cooling rates. It was proposed that when samples

Fig. 5. (a-h) Modeled time-temperature paths for the analyzed samples from the Pulang complex conducted using HeFTy modeling of Ketcham (2005). The green area in each plot denotes the envelope for all acceptable time-temperature paths with a goodness of fit >0.05, whereas the purple areas encompass all good time-temperature paths with a goodness fit of >0.6. The thick black line enveloped in the pink region depicts the weighted mean cooling path for each plot. The regions of helium partial retention zone for apatite (AHePRZ) and helium partial retention zone for zircon (ZHePRZ) were calculated using the CLOSURE program of Brandon et al. (1998) at a hold time of 50 m.y., based on the size of analyzed zircon and apatite crystals (Electronic App. Tables A3, A4).
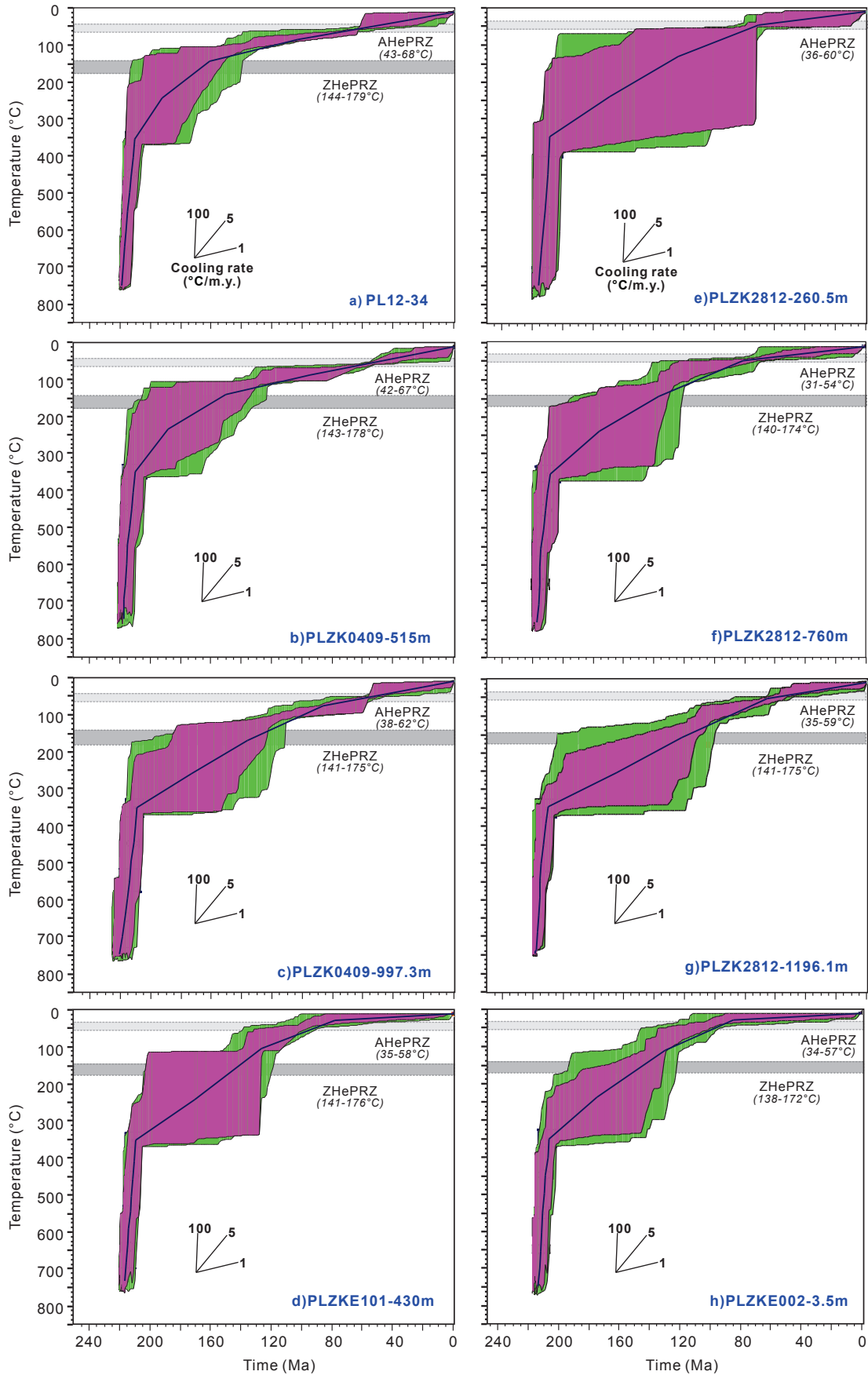
Table 3. Summary of Inverse Thermal Modeling Results for Four Samples from the Pulang Complex

Parameter \ Sample	PL12-34	PLZK0409-515m	PLZK2812-760m	PLZK2812-260.5m
Age of emplacement (Ma)	217.0	216.4	215.2	215.2
Emplacement depth[1] (km)	5.0–5.5	5.5–6.0	6.5	5.5–6.0
Age of deposit cooled[2] (Ma)	212.6–211.6	211.2–211.1	208.8	209–208.9
Magmatic cooling rate[3] (°C/m.y.)	124–139	138–140	112	117–119
Exhumation cooling rate[4] (°C/m.y.)	1.18–1.19	1.27	1.4	1.25–1.27
Duration of 500°–300°C interval (m.y.)	0.56–1.08	1.49–1.58	4.14	2.27–2.34
Exhumation rate of intrusion[5] (m/m.y.)	14.4–16.8	2.2–11	5	4.8–10.1
Exhumation rate of country rock[6] (m/m.y.)	32.7–32.9	33.7	45	39
Age of exposure at paleosurface[7] (Ma)	65–48.9	53–38	70.8	74.3–61.5
Estimated thickness of intrusion[8] (m)	706–1,092	599–1,099	794	558–1,010

Detailed description of parameters can be found in McInnes et al. (2005a) and Fu et al. (2010)
[1]Emplacement depth is defined as the distance from the paleosurface to the top of the igneous body
[2]The igneous body has cooled when it reaches the same temperature as the surrounding country rock
[3]Magmatic cooling refers to the cooling from emplacement to the cooled state as defined above
[4]Exhumation cooling refers to the interval from the cooled state through cooling to surface temperature of 10°C
[5]Exhumation rate of intrusion refers to the average exhumation rate for the intrusion from the emplacement to the paleosurface
[6]Exhumation rate of country rock refers to the average exhumation rate for the country rocks from deep to the paleosurface
[7]Age of exposure is defined as the age when the top of the igneous body is exposed to the paleosurface
[8]Estimated eroded thickness refers to the eroded thickness of the intrusion since it was exposed to the paleosurface

are slowly cooled or resident in the helium partial retention zones for protracted periods, diffusion can magnify the differences in He concentrations for different-sized crystals (especially for small crystals). Consequently, the age variation between different crystals becomes greater (e.g., Meesters and Dunai, 2002; Fitzgerald et al., 2006). The modeled results from HeFTy and 4DTherm suggest a protracted and extremely slow cooling since the Early Cretaceous (Figs. 5, 6), probably giving rise to a comparatively greater variation in the single-grain apatite (U-Th)/He ages. In contrast, the moderate cooling from the Late Triassic to Early Cretaceous led to a smaller variation in the single-grain zircon (U-Th)/He ages.

Formation and duration of the Pulang porphyry system

Porphyry deposits are produced by dynamically evolving magmatic-hydrothermal systems (e.g., Sillitoe, 2010).
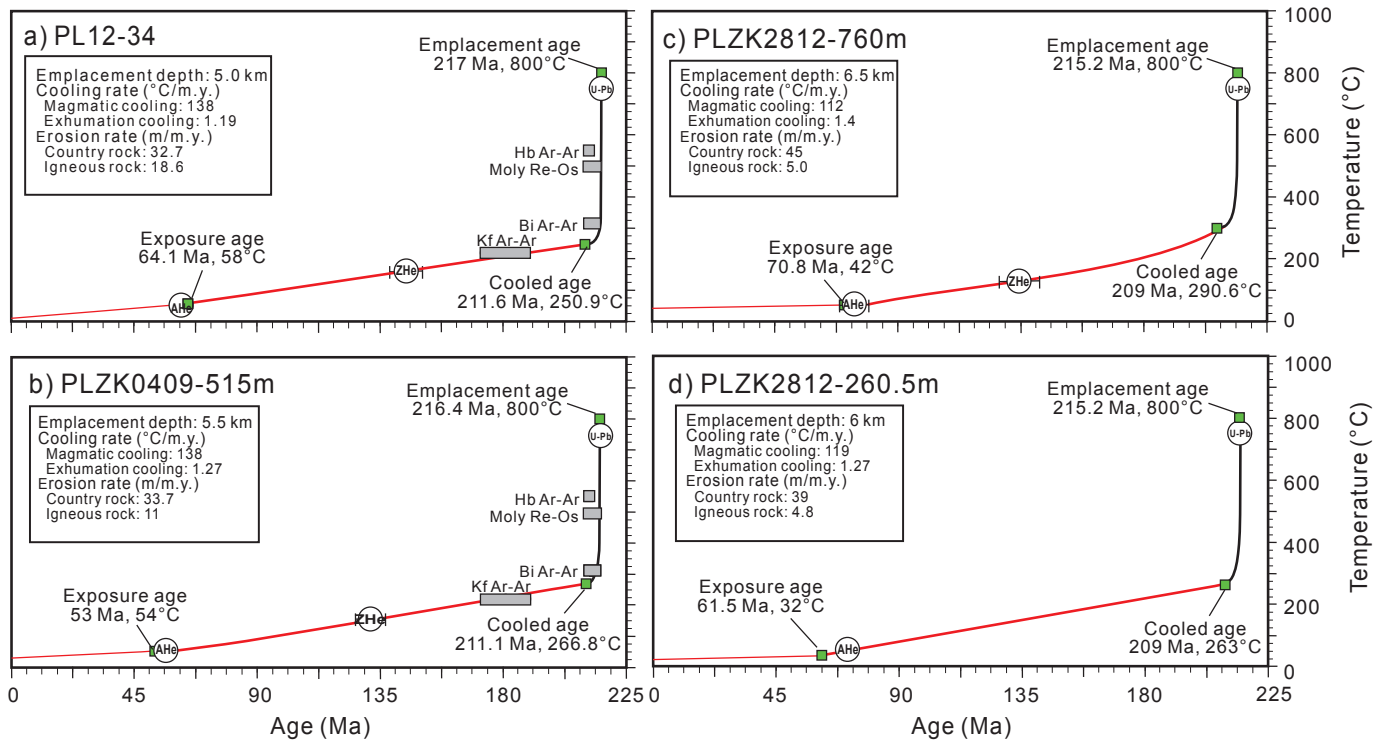

Fig. 6. (a-d) Graphic depiction of modeling results for some representative samples from the Pulang complex obtained using 4DTherm of Fu et al. (2010). The previously published Ar-Ar and Re-Os ages (Table 1) are also plotted in the left two figures for comparison. Abbreviations: AHe = apatite (U-Th)/He, Bi = biotite, Hb = hornblende, Kf = K-feldspar, Moly = molybdenite, ZHe = zircon (U-Th)/He.
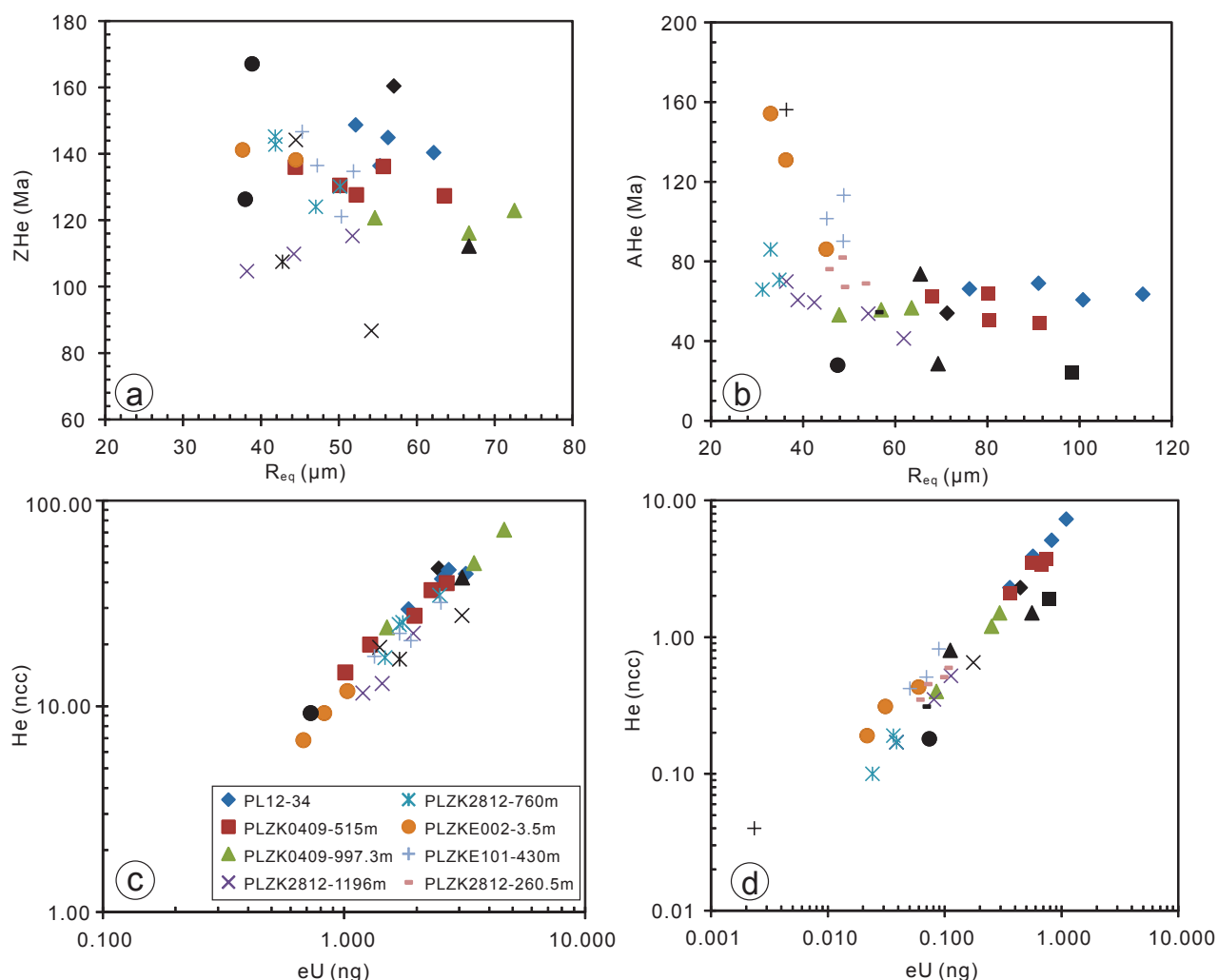
Fig. 7. Plots of zircon (U-Th)/He (ZHe) and apatite (U-Th)/He (AHe) ages vs. equivalent spherical radius (R_{eq}) (a, b) and helium content vs. eU concentration (c, d) for zircon and apatite grains from the Pulang complex. eU = U + 0.235Th. Note that the symbols in black denote the outliers detected by Chauvenet's criterion.

Understanding the duration of genetic magmatic-hydrothermal processes is fundamental to exploring the mechanisms of porphyry deposit formation (McInnes et al., 2005a, b; Chiaradia et al., 2009, 2013; von Quadt et al., 2011; Buret et al., 2016, 2017). The suite of radiometric ages obtained in this study (Table 2), combined with previously published geochronological and thermochronological data for the Pulang deposit (Table 1), places good temporal constraints on the initiation and duration of magmatic-hydrothermal activity at Pulang. The new zircon U-Pb data (217.6 ± 1.3–213.5 ± 1.9 Ma) provide additional constraints on the timing of emplacement of the Pulang complex.

Zircon (U-Th)/He ages (T_c = 183°C, at 10°C/m.y.; Reiners et al., 2004) have been used to temporally constrain the termination of a magmatic-hydrothermal event (e.g., McInnes et al., 2005a, b; Fu et al., 2010; Braxton et al., 2012) and can be combined with zircon U-Pb ages to reveal the duration of hypogene ore formation. However, this approach is not suitable for Pulang. As shown in Table 2 and Figure 4, the zircon (U-Th)/He ages display a wide range (142–110 Ma) and generally show a positive correlation with elevation,

suggesting that the Pulang complex was emplaced at depths below 4.5 to 6.0 km (assuming a geothermal gradient of 30°–40°C/km), where the ambient temperature exceeds the helium blocking temperature for zircon. Our inverse thermal modeling also yielded a similar emplacement depth (5.0–6.5 km) for the complex. In this scenario, the zircon (U-Th)/He age records the cooling time of when the sample was uplifted and cooled through the He closure temperature. The biotite [40]Ar/[39]Ar system has a T_c of 310 ± 20°C (Harrison et al., 1985), which is similar to the lower-temperature limit of magmatic-hydrothermal activity. We therefore propose that it presents a plausible proxy for bracketing the duration of the magmatic-hydrothermal system for deep-seated porphyry intrusions. Three biotite [40]Ar/[39]Ar plateau ages from 214.6 ± 0.9 to 210.3 ± 0.8 Ma have been presented by previous workers (i.e., Zeng et al., 2006; Wang, 2008; Li et al., 2011; Table 1). Combined with the new zircon U-Pb ages, it is estimated that magmatic-hydrothermal activity lasted at least 3 to 7 m.y. This long time scale is also supported by inverse thermal modeling results (Table 3; Figs. 5, 6). Recent precise geochronological studies of porphyry deposits worldwide have indicated

that deposits may form within tens of thousands of years (e.g., Henry et al., 1997; Shinohara and Hedenquist, 1997; Pollard et al., 2005; von Quadt et al., 2011; Chiaradia et al, 2013; Buret et al., 2016, 2017) or several million years (e.g., Ballard et al., 2001; Maksaev et al., 2006; Harris et al., 2008; Sillitoe and Mortensen, 2010; Barra et al., 2013; Deckart et al., 2013, 2014, and references therein; Leng et al., 2013). These long-lived magmatic-hydrothermal events are typically attributed to episodic buildup and evolution of the underlying more voluminous pluton that feeds the upper crustal porphyritic intrusive complex (e.g., Sillitoe, 2010; Sillitoe and Mortensen, 2010; Chelle-Michou et al., 2014; Chiaradia and Caricchi, 2017; Leng et al., 2018).

Thermal and erosion history of the Pulang deposit

In this study, two different inverse thermal modeling programs (i.e., HeFTy and 4DTherm) were independently utilized to reconstruct the cooling and exhumation histories of the analyzed samples. In general, the time-temperature cooling paths determined by both programs are consistent (Figs. 5, 6), despite minor differences in inflection points. Moreover, the cooling curves in Figure 6 also match the previous published radiometric ages within error, indicating that the modeled cooling paths are reliable. As a whole, the curves in Figure 6 show a typical hockey-stick pattern that is generally attributed to a slowly cooled, deep pluton (e.g., McInnes et al., 2005a). Our modeling yielded an emplacement depth below 5.0 km. In addition, at least three distinct cooling stages can be recognized from the time-temperature cooling curves (Figs. 5, 6). The first stage of rapid cooling in the Late Triassic was related to cooling of the magma by advective heat loss and convection (Cathles, 1981). This process lasted approximately 3 to 7 m.y. as constrained by the zircon U-Pb ages and modeling results (Figs. 5, 6; Table 3).

Both the second and the third stages of cooling at Pulang were primarily controlled by erosion and exhumation processes. Moreover, the decrease in the cooling rate (i.e., from ~3°–5°C/m.y. in the second stage to less than 1°C/m.y. in the third stage) could be related to a decrease in the erosion rate during the third phase, consistent with the results derived from the age-elevation relationships (Fig. 4). Collectively, these results imply that Pulang has undergone at least two stages of exhumation (Fig. 8). The early-stage erosion was

initiated no later than 182 m.y. ago based on the K-feldspar $^{40}Ar/^{39}Ar$ plateau age (Wang, 2008), probably as early as the Late Triassic, and lasted until the Late Cretaceous. During this stage, the country rocks were exhumed at a rate of 33 to 45 m/m.y. The estimated thickness of eroded country rock was more than 5.0 km. The Pulang complex was probably exposed to paleosurface between the Late Cretaceous and Early Eocene, based on the results of our modeling. The late stage continued to the present day, unroofing the Pulang complex at a much slower rate of 5 to 17 m/m.y., with ~558- to 1,099-m thicknesses of materials removed likely. A substantial amount of ore from the Pulang deposit was probably removed during uplift and erosion, given that the Cu-bearing stockwork veins are exposed at surface (Fig. 2b). The long-term (>50 m.y.) exposure of the Pulang mineralization, combined with the moderate to strong rainfall in this region, inhibited supergene enrichment of the deposit.

Implications for the preservation of ancient porphyry systems in southeastern Tibet

It is suggested that the entire Yidun terrane, as well as broader southeastern Tibet, cooled below 300°C since the Late Triassic (~199 Ma) and experienced a long period (>100 m.y.) of thermal stability from the Jurassic to early Paleogene (e.g., Reid et al., 2005; Roger et al., 2011; Tian et al., 2014). Our dating results from the Pulang complex provide more detailed insights into the Cenozoic thermal evolution of this region, which involved an early stage of relatively rapid erosion and a late stage of much slower erosion. This decrease in cooling rate in the Yidun terrane was previously considered to be a result of crustal refrigeration due to the subduction of the Meso-Tethanys and the subsequent collision between the Lhasa and Qiangtang terranes in the Cretaceous (e.g., Tian et al., 2014). Kapp et al. (2005) has demonstrated that the Cretaceous collision of the Lhasa and Qiangtang terranes resulted in substantial shortening and thickening of the upper crustal rocks, causing regional uplift of the eastern Tibetan Plateau during the early Paleogene (~45 Ma; Rohrmann et al., 2012). However, this is not the case in the Yidun terrane. Considering the geomorphic features and thermal evolution of the Yidun terrane, we therefore suggest that moderate cooling in the upper crustal rocks from the Late Triassic to Early Cretaceous as recorded
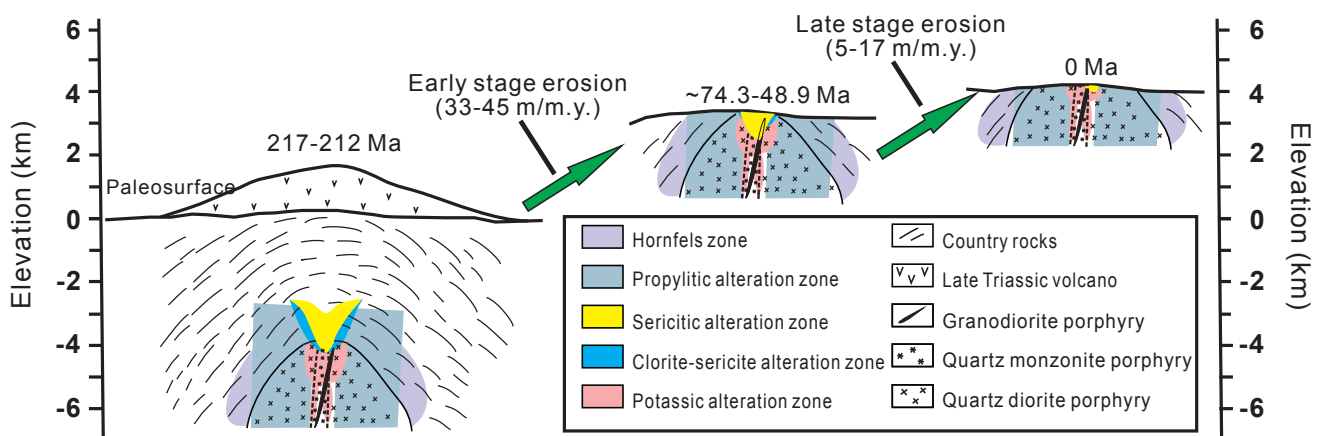

Fig. 8. Schematic diagram showing the uplift and denudation history of the Pulang deposit. See text for details.

by the Pulang complex resulted from isostatic adjustment of the crust after the subduction of the Ganz-Litang Ocean beneath the Yidun terrane in the Late Triassic (Leng et al., 2014). A low-relief paleosurface landscape (i.e., peneplain), probably at low altitude, formed during the Late Cretaceous. The slow crustal cooling rate and extremely slow erosion rate from Late Cretaceous to the present day was a response to the presence of this peneplain landscape.

A number of low-temperature thermochronological studies from several large rivers (e.g., Yalong, Dadu, and Jinsha Rivers) that dissect the Yidun terrane indicated that rapid river incision of 200 to 500 m/m.y. started around 15 to 9 Ma (e.g., Clark et al., 2005; Ouimet et al., 2010). This rapid incision was considered to be a response to the nearly coeval rapid uplift of the entire southeastern Tibetan Plateau. Clark et al. (2005) invoked a lower crustal and mantle channel flow model to explain the uplift of the southeastern Tibetan Plateau. However, this model was recently challenged by several studies from adjacent areas that demonstrate that the onset of surface uplift commenced from late Oligocene to early Miocene (30–15 Ma; e.g., Wang et al., 2012; Tian et al., 2014). These obvious discrepancies in the uplift history from different sites strongly support a stepwise uplift geodynamic model (Tapponnier et al., 2001). The prolonged period of extremely slow cooling and denudation of the Pulang complex indicates that the porphyry system was not affected by rapid Miocene denudation. Therefore, the Miocene rapid uplift was not propagated to the entire Tibetan Plateau but was likely restricted to some major faults (e.g., Roger et al., 2011; Zhang et al., 2015, 2017).

In summary, we propose that the presence of a relict peneplain in modern southeast Tibetan Plateau was favorable for preservation of the Triassic Pulang porphyry deposit. Our results may also provide new insights into the preservation of other ancient porphyry deposits in the pre-Mesozoic orogenic belts, such as the Devonian Oyu Tolgoi porphyry Cu-Au deposits in the Central Asian orogenic belt (e.g., Wainwright et al., 2017) and the Silurian Cadia porphyry Au-Cu clusters in the Lachlan fold belt (e.g., Holliday et al., 2002).

Concluding Remarks

U-Pb-He dating and numerical modeling suggest that the Pulang intrusive complex was emplaced at a paleodepth of 5.0 to 6.5 km around 215 ± 2 Ma. The relatively deep level emplacement of the complex, coupled with the episodic replenishment of the magma chamber, accounts for prolonged magmatic-hydrothermal activity at Pulang.

Three phases of cooling were revealed by the thermal history modeling at Pulang, including a rapid cooling phase in the Late Triassic, a moderate cooling from the Late Triassic to Early Cretaceous, and a monotonic and extremely slow cooling from the Early Cretaceous to the present day. The early, first phase of cooling mainly reflects magmatic cooling processes, whereas the later two phases of cooling were predominantly controlled by erosion and exhumation processes. Moreover, the decrease in cooling rate from the second to the third phase could be related to a decreasing erosion rate. Overall, our results indicate that the Pulang complex has experienced at least two stages of exhumation at rates of 33 to 45 m/m.y. and 5 to 17 m/m.y., respectively. Moreover, it is estimated that

a substantial amount of ore from the Pulang deposit was probably removed during uplift and erosion processes.

The Triassic Pulang deposit has undergone long-term (>50 m.y.), extremely slow cooling (<1°C/m.y.) and denudation since the Late Cretaceous and was not affected by the rapid incision in the late Miocene. This is probably related to the formation of a relict peneplain on the southeastern Tibetan Plateau from the Cretaceous that has survived to the present day.

REFERENCES

Baker, J., Peate, D., Waight, T., and Meyzen, C., 2004, Pb isotopic analysis of standards and samples using a 207Pb-204Pb double spike and thallium to correct for mass bias with a double-focusing MC-ICP-MS: Chemical Geology, v. 211, p. 275–303.

Ballard, J.R., Palin, J.M., Williams, I.S., Campbell, I.H., and Faunes, A., 2001, Two ages of porphyry intrusion resolved for the super-giant Chuquicamata copper deposit of northern Chile by ELA-ICP-MS and SHRIMP: Geology, v. 29, p. 383–386.

Barra, F., Alcota, H., Rivera, S., Valencia, V., Munizaga, F., and Maksaev, V., 2013, Timing and formation of porphyry Cu-Mo mineralization in the Chuquicamata district, northern Chile: New constraints from the Toki cluster: Mineralium Deposita, v. 48, p. 629–651.

Bineli Betsi, T., Lentz, D., McInnes, B., and Evans, N.J., 2012, Emplacement ages and exhumation rates for intrusion-hosted Cu-Mo-Sb-Au mineral systems at Freegold Mountain (Yukon, Canada): Assessment from U-Pb, Ar-Ar, and (U-Th)/He geochronometers: Canadian Journal of Earth Sciences, v. 49, no. 5, p. 653–670.

Black, L.P., Kamo, S.L., Allen, C.M., Aleinikoff, J.N., Davis, D.W., Korsch, R.J., and Foudoulis, C., 2003, TEMORA 1: A new zircon standard for Phanerozoic U-Pb geochronology: Chemical Geology, v. 200, p. 155–170.

Brandon, M.T., Roden-Tice, M.K., and Garver, J.I., 1998, Late Cenozoic exhumation of the Cascadia accretionary wedge in the Olympic Mountains, northwest Washington state: Geological Society of America Bulletin, v. 110, p. 985–1009.

Braxton, D.P., Cooke, D.R., Dunlap, J., Norman, M., Reiners, P., Stein, H., and Waters, P., 2012, From crucible to graben in 2.3 Ma: A high-resolution geochronological study of porphyry life cycles, Boyongan-Bayugo copper-gold deposits, Philippines: Geology, v. 40, p. 471–474.

Buret, Y., von Quadt, A., Heinrich, C., Selby, D., Wälle, M., and Peytcheva, I., 2016, From a long-lived upper-crustal magma chamber to rapid porphyry copper emplacement: Reading the geochemistry of zircon crystals at Bajo de la Alumbrera (NW Argentina): Earth and Planetary Science Letters, v. 450, p. 120–131.

Buret, Y., Wotzlaw, J.-F., Roozen, S., Guillong, M., von Quadt, A., and Heinrich, C.A., 2017, Zircon petrochronological evidence for a plutonic-volcanic connection in porphyry copper deposits: Geology, v. 45, p. 623–626.

Cathles, L.M., 1981, Fluid flow and genesis of hydrothermal ore deposits: Economic Geology 75th Anniversary Volume, p. 424–457.

Chang, E.Z., 2000, Geology and tectonics of the Songpan-Ganzi fold belt, southwestern China: International Geology Review, v. 42, p. 813–831.

Chelle-Michou, C., Chiaradia, M., Ovtcharova, M., Ulianov, A., and Wotzlaw, J.-F., 2014, Zircon petrochronology reveals the temporal link between porphyry systems and the magmatic evolution of their hidden plutonic roots (the Eocene Coroccohuayco deposit, Peru): Lithos, v. 198–199, p. 129–140.

Chiaradia, M., and Caricchi, L., 2017, Stochastic modelling of deep magmatic controls on porphyry copper deposit endowment: Scientific Reports, v. 7, article no. 44523, doi: 10.1038/srep44523.

Chiaradia, M., Merino, D., and Spikings, R., 2009, Rapid transition to long-lived deep crustal magmatic maturation and the formation of giant porphyry-related mineralization (Yanacocha, Peru): Earth and Planetary Science Letters, v. 288, p. 505–515.

Chiaradia, M., Schaltegger, U., Spikings, R., Wotzlaw, J.-F., and Ovtcharova, M., 2013, How accurately can we date the duration of magmatic-hydrothermal events in porphyry systems?—an invited paper: Economic Geology, v. 108, p. 565–584.

Clark, M.K., House, M.A., Royden, L.H., Whipple, K.X., Burchfiel, B.C., Zhang, X., and Tang, W., 2005, Late Cenozoic uplift of southeastern Tibet: Geology, v. 33, p. 525–528.

Cooke, D.R., Hollings, P., Wilkinson, J.J., and Tosdal, R.M., 2014. Geochemistry of porphyry deposits, *in* Holland, H.D., and Turekian, K.K., eds., Treatise on geochemistry, 2nd ed.: Oxford, Elsevier, p. 357–381.

Danišík, M., McInnes, B.I.A., Kirkland, C., McDonald, B.J., Evans, N.J., and Becker, T., 2017, Seeing is believing: Visualization of He distribution in zircon and implications for thermal history reconstruction on single crystals: Science Advances, v. 3, e1601121.

Deckart, K., Clark, A.H., Cuadra, P., and Fanning, M., 2013, Refinement of the time-space evolution of the giant Mio-Pliocene Río Blanco-Los Bronces porphyry Cu-Mo cluster, central Chile: New U-Pb (SHRIMP II) and Re-Os geochronology and ⁴⁰Ar/³⁹Ar thermochronology data: Mineralium Deposita, v. 48, p. 57–79.

Deckart, K., Silva, W., Spröhnle, C., and Vela, I., 2014, Timing and duration of hydrothermal activity at the Los Bronces porphyry cluster: An update: Mineralium Deposita, v. 49, p. 535–546.

Ehlers, T.A., Chaudhri, T., Kumar, S., Fuller, C.W., Willett, S.D., Ketcham, R.A., Belton, D.X., Kohn, B.P., Gleadow, A.J.W., and Dunai, T.J., 2005, Computational tools for low-temperature thermochronometer interpretation: Reviews in Mineralogy and Geochemistry, v. 58, p. 589–562.

Evans, N.J., Byrne, J.P., Keegan, J.T., and Dotter, L.E., 2005, Determination of uranium and thorium in zircon, apatite, and fluorite: Application to laser (U-Th)/He thermochronology: Journal of Analytical Chemistry, v. 60, p. 1159–1165.

Evans, N.J., McInnes, B.I.A., McDonald, B., Danišík, M., Jourdan, F., Mayers, C., Thern, E., and Corbett, D., 2013, Emplacement age and thermal footprint of the diamondiferous Ellendale E9 lamproite pipe, Western Australia: Mineralium Deposita, v. 48, p. 413–421.

Fan, Y.H., and Li, W.C., 2006, Geological characteristics of the Pulang porphyry copper deposit, Yunnan: Geology in China, v. 33, p. 352–362 (in Chinese with English abs.).

Farley, K.A., 2000, Helium diffusion from apatite: General behavior as illustrated by Durango fluorapatite: Journal of Geophysical Research Atmospheres, v. 105, p. 2903–2914.

Farley, K.A., House, M.A., and Kohn, B.P., 1998, Laboratory and natural diffusivity calibrations for apatite (U-Th)/He thermochronometry: Mineralogical Magazine, v. 62A, p. 436–437.

Fitzgerald, P.G., Baldwin, S.L., Webb, L.E., and O'Sullivan, P.B., 2006, Interpretation of (U-Th)/He single grain ages from slowly cooled crustal terranes: A case study from the Transantarctic Mountains of southern Victoria Land: Chemical Geology, v. 225, p. 91–120.

Flowers, R.M., and Farley, K.A., 2012, Apatite ⁴He/³He and (U-Th)/He evidence for an ancient Grand Canyon: Science, v. 338, p. 1616–1619.

Flowers, R.M., Ketcham, R.A., Shuster, D.L., and Farley, K.A., 2009, Apatite (U-Th)/He thermochronometry using a radiation damage accumulation and annealing model: Geochimica et Cosmochimica Acta, v. 73, p. 2347–2365.

Foland, K.A., 1994, Argon diffusion in feldspars, *in* Parsons, I., ed., Feldspars and their reactions: Dordrecht, Springer Netherlands, p. 415–447.

Fu, F.Q., McInnes, B.I.A., Evans, N.J., and Davies, P.J., 2010, Numerical modeling of magmatichydrothermal systems constrained by U-Th-Pb-He time-temperature histories: Journal of Geochemical Exploration, v. 106, p. 90–109.

Guenthner, W.R., Reiners, P.W., Ketcham, R.A., Nasdala, L., and Giester, G., 2013, Helium diffusion in natural zircon: Radiation damage, anisotropy, and the interpretation of zircon (U-Th)/He thermochronology: American Journal of Science, v. 313, p. 145–198.

Harris, A.C., Dunlap, W.J., Reiners, P.W., Allen, C.M., Cooke, D.R., White, N.C., Campbell, I.H., and Golding, S.D., 2008, Multimillion year thermal history of a porphyry copper deposit: Application of U-Pb, ⁴⁰Ar/³⁹Ar

and (U-Th)/He chronometers, Bajo de la Alumbrera copper-gold deposit, Argentina: Mineralium Deposita, v. 43, p. 295–314.

Harrison, T.M., Duncan, I., and McDougall, I., 1985, Diffusion of ⁴⁰Ar in biotite: Temperature, pressure and compositional effects: Geochimica et Cosmochimica Acta, v. 49, p. 2461–2468.

Henry, C.D., Elson, H.B., McIntosh, W.C., Heizler, M.T., and Castor, S.B., 1997, Brief duration of hydrothermal activity at Round Mountain, Nevada, determined from ⁴⁰Ar/³⁹Ar geochronology: Economic Geology, v. 92, p. 807–826.

Holliday, J.R., Wilson, A.J., Blevin, P.L., Tedder, I.J., Dunham, P.D., and Pfitzner, M., 2002, Porphyry gold-copper mineralisation in the Cadia district, eastern Lachlan fold belt, New South Wales, and its relationship to shoshonitic magmatism: Mineralium Deposita, v. 37, p. 100–116.

Jackson, S.E., Pearson, N.J., Griffin, W.L., and Belousova, E.A., 2004, The application of laser ablation-inductively coupled plasma-mass spectrometry to in situ U-Pb zircon geochronology: Chemical Geology, v. 211, p. 47–69.

Kapp, P., Yin, A., Harrison, T.M., and Ding, L., 2005, Cretaceous-Tertiary shortening, basin development, and volcanism in central Tibet: Geological Society of America Bulletin, v. 117, p. 865–878.

Ketcham, R.A., 2005, Forward and inverse modeling of low-temperature thermochronometry data: Reviews in Mineralogy and Geochemistry, v. 58, p. 275–314.

Leng, C.B., Zhang, X.C., Zhong, H., Hu, R.Z., Zhou, W.D., and Li, C., 2013, Re-Os molybdenite ages and zircon Hf isotopes of the Gangjiang porphyry Cu-Mo deposit in the Tibetan orogen: Mineralium Deposita, v. 48, p. 585–602.

Leng, C.B., Huang, Q.Y., Zhang, X.C., Wang, S.X., Zhong, H., Hu, R.Z., Bi, X.W., Zhu, J.J., and Wang, X.S., 2014, Petrogenesis of the Late Triassic volcanic rocks in the southern Yidun arc, SW China: Constraints from the geochronology, geochemistry, and Sr-Nd-Pb-Hf isotopes: Lithos, v. 190, p. 363–382.

Leng, C.B., Gao, J.F., Chen T.W., Zhang, X.C., Tian, Z.D., and Guo, J.H., 2018, Platinum-group elements, zircon Hf-O isotopes, and mineralogical constraints on magmatic evolution of the Pulang porphyry Cu-Au system, SW China: Gondwana Research, doi: 10.1016/j.gr.2018.03.001.

Li, W.C., Yin, G.H., Lu, Y.X., Liu, X.L., Dong, X.U., and Zhang, S.Q., 2009, The evolution and ⁴⁰Ar-³⁹Ar isotopic evidence of the Pulang complex in Zhongdian: Acta Geologica Sinica, v. 83, p. 1421–1429 (in Chinese with English abs.).

Li, W.C., Zeng, P.S., Hou, Z.Q., and White, N.C., 2011, The Pulang porphyry copper deposit and associated felsic intrusions in Yunnan Province, southwest China: Economic Geology, v. 106, p. 79–92.

Liu, X., Li, W., Yin, G., and Zhang, N., 2013, The geochronology, mineralogy, and geochemistry study of the Pulang porphyry copper deposits in Geza arc of Yunnan province: Acta Petrologica Sinica, v. 29, p. 3049–3064 (in Chinese with English abs.).

Liu, X., Fan, H.R., Evans, N.J., Yang, K.F., Danišík, M., Mcinnes, B.I.A., Qin, K.Z., and Yu, X.F., 2017, Exhumation history of the Sanshandao Au deposit, Jiaodong: Constraints from structural analysis and (U-Th)/He thermochronology: Scientific Reports, v. 7, no. 7787, doi: 10.1038/s41598-017-08103-w.

Maksaev, V., Munizaga, F., Fanning, M., Palacios, C., and Tapia, J., 2006, SHRIMP U-Pb dating of the Antucoya porphyry copper deposit: New evidence for an Early Cretaceous porphyry-related metallogenic epoch in the Coastal Cordillera of northern Chile: Mineralium Deposita, v. 41, p. 637–644.

Masterman, G.J., Cooke, D.R., Berry, R.F., Walshe, J.L., Lee, A.W., and Clark, A.H., 2005, Fluid chemistry, structural setting, and emplacement history of the Rosario Cu-Mo porphyry and Cu-Ag-Au epithermal veins, Collahuasi district, northern Chile: Economic Geology, v. 100, p. 835–862.

McDowell, F.W., Mcintosh, W.C., and Farley, K.A., 2005, A precise ⁴⁰Ar-³⁹Ar reference age for the Durango apatite (U-Th)/He and fission-track dating standard: Chemical Geology, v. 214, p. 249–263.

McInnes, B.I.A., Farley, K.A., Sillitoe, R.H., and Kohn, B.P., 1999, Application of apatite (U-Th)/He thermochronometry to the determination of the sense and amount of vertical fault displacement at the Chuquicamata porphyry copper deposit, Chile: Economic Geology, v. 94, p. 937–947.

McInnes, B.I.A., Evans, N.J., Fu, F.Q., and Garwin, S., 2005a, Application of thermochronology to hydrothermal ore deposits: Reviews in Mineralogy and Geochemistry, v. 58, p. 467–498.

McInnes, B.I.A., Evans, N.J., Fu, F.Q., Garwin, S., Belousova, E., Griffin, W.L., Bertens, A., Sukarna, D., Permanadewi, S., Andrew, R.L., and Deckart, K., 2005b, Thermal history analysis of selected Chilean, Indonesian, and Iranian porphyry Cu-Mo-Au deposits, *in* Porter, T.M., ed., Superporphyry

copper and gold deposits—a global perspective: Adelaide, PGC Publishing, p. 367–386.

McInnes, B.I.A., Evans, N.J., Mcdonald, B.J., Kinny, P.D., and Jakimowicz, J., 2009, Zircon U-Th-Pb-He double dating of the Merlin kimberlite field, Northern Territory, Australia: Lithos, v. 112, p. 592–599.

Meesters, A.G.C.A., and Dunai, T.J., 2002, Solving the production-diffusion equation for finite diffusion domains of various shapes: Part II. Application to cases with α-ejection and nonhomogeneous distribution of the source: Chemical Geology, v. 41, p. 817–834.

Meffre, S., Large, R.R., Scott, R., Woodhead, J., Chang, Z., Gilbert, S.E., Danyushevsky, L.V., Maslennikov, V., and Hergt, J.M., 2008, Age and pyrite Pb isotopic composition of the giant Sukhoi Log sediment-hosted gold deposit, Russia: Geochimica et Cosmochimica Acta, v. 72, p. 2377–2391.

Ouimet, W., Whipple, K., Royden, L., Reiners, P., Hodges, K., and Pringle, M., 2010, Regional incision of the eastern margin of the Tibetan Plateau: Lithosphere, v. 2, p. 50–63.

Pang, Z.S., Du, Y S., Wang, G W., Guo, X., Cao, Y., and Li, Q., 2009, Single-grain zircon U-Pb isotopic ages, geochemistry and its implication of the Pulang complex in Yunnan Province, China: Acta Petrologica Sinica, v. 25, p. 159–165 (in Chinese with English abs.).

Pollard, P.J., Taylor, R.G., and Peters, L., 2005, Ages of intrusion, alteration, and mineralization at the Grasberg Cu-Au deposit, Papua, Indonesia: Economic Geology, v. 100, p. 1005–1020.

Reid, A., Wilson, C.J.L., Shun, L., Pearson, N., and Belousova, E., 2007, Mesozoic plutons of the Yidun arc, SW China: U/Pb geochronology and Hf isotopic signature: Ore Geology Reviews, v. 31, p. 88–106.

Reid, A.J., Wilson, C.J.L., Phillips, D., and Liu, S., 2005, Mesozoic cooling across the Yidun arc, central-eastern Tibetan Plateau: A reconnaissance $^{40}Ar/^{39}Ar$ study: Tectonophysics, v. 398, p. 45–66.

Reiners, P.W., 2005, Zircon (U-Th)/He Thermochronometry: Reviews in Mineralogy and Geochemistry, v. 58, p. 151–179.

Reiners, P.W., and Brandon, M.T., 2006, Using thermochronology to understand orogenic erosion: Annual Review of Earth and Planetary Sciences, v. 34, p. 419–466.

Reiners, P.W., Ehlers, T.A., Mitchell, S.G., and Montgomery, D.R., 2003, Coupled spatial variations in precipitation and long-term erosion rates across the Washington Cascades: Nature, v. 426, p. 645–647.

Reiners, P.W., Spell, T.L., Nicolescu, S., and Zanetti, K.A., 2004, Zircon (U-Th)/He thermochronometry: He diffusion and comparisons with $^{40}Ar/^{39}Ar$ dating: Geochimica et Cosmochimica Acta, v. 68, p. 1857–1887.

Richards, J.P., 2011, Magmatic to hydrothermal metal fluxes in convergent and collided margins: Ore Geology Reviews, v. 40, p. 1–26.

Roger, F., Jolivet, M., Cattin, R., and Malavieille, J., 2011, Mesozoic-Cenozoic tectonothermal evolution of the eastern part of the Tibetan Plateau (Songpan-Garze, Longmen Shan area): Insights from thermochronological data and simple thermal modelling: Geological Society London Special Publications, v. 353, p. 9–25.

Rohrmann, A., Kapp, P., Carrapa, B., Reiners, P.W., Guynn, J., Ding, L., and Heizler, M., 2012, Thermochronologic evidence for plateau formation in central Tibet by 45 Ma: Geology, v. 40, p. 187–110.

Sack, P.J., Berry, R.F., Sebastien, M., Falloon, T.J., Bruce, G.J., and Friedman, R.M., 2011, In situ location and U-Pb dating of small zircon grains in igneous rocks using laser ablation-inductively coupled plasma-quadrupole mass spectrometry: Geochemistry Geophysics Geosystems, v. 12, p. 99–108.

Shinohara, H., and Hedenquist, J.W., 1997, Constraints on magma degassing beneath the Far Southeast porphyry Cu-Au deposit, Philippines: Journal of Petrology, v. 38, p. 1741–1752.

Sillitoe, R.H., 2010, Porphyry copper systems: Economic Geology, v. 105, p. 3–41.

Sillitoe, R.H., and Mortensen, J.K., 2010, Longevity of porphyry copper formation at Quellaveco, Peru: Economic Geology, v. 105, p. 1157–1162.

Singer, D.A., Berger, V.I., and Moring, B.C., 2008, Porphyry copper deposits of the world: Satabase and grade and tonnage models, 2008: U.S. Geological Survey, Open-File Report 2008–1155, https://pubs.er.usgs.gov/publication/ofr20081155.

Song, X.Y., Zhou, M.F., Cao, Z.M., and Robinson, P.T., 2004, Late Permian rifting of the South China craton caused by the Emeishan mantle plume?: Journal of the Geological Society, v. 161, p. 773–781.

Stacey, J.S., and Kramers, J.D., 1975, Approximation of terrestrial lead isotope evolution by a two-stage model: Earth and Planetary Science Letters, v. 26, p. 207–221.

Tapponnier, P., Xu, Z.Q., Roger, F., Meyer, B., Arnaud, N., Wittlinger, G., and Yang, J.S., 2001, Oblique stepwise rise and growth of the Tibet Plateau: Science, v. 294, p. 1671–1677.

Tian, Y., Kohn, B.P., Gleadow, A.J.W., and Hu, S., 2014, A thermochronological perspective on the morphotectonic evolution of the southeastern Tibetan Plateau: Journal of Geophysical Research: Solid Earth, v. 119, p. 676–698.

Villa, I., and Hanchar, J., 2013, K-feldspar hygrochronology: Geochimica et Cosmochimica Acta, v. 101, p. 24–33.

von Quadt, A., Erni, M., Martinek, K., Moll, M., Peytcheva, I., and Heinrich, C.A., 2011, Zircon crystallization and the lifetimes of ore-forming magmatic-hydrothermal systems: Geology, v. 39, p. 731–734.

Wagner, G.A., and Reimer, G.M., 1972, Fission track tectonics: The tectonic interpretation of fission track apatite ages: Earth and Planetary Science Letters, v. 14, p. 263–268.

Wainwright, A.J., Tosdal, R.M., Lewis, P.D., and Friedman, R.M., 2017, Exhumation and preservation of porphyry Cu-Au deposits at Oyu Tolgoi, South Gobi region, Mongolia: Economic Geology, v. 112, p. 591–601.

Wang, B.Q., Zhou, M.F., Li, J.W., and Yan, D.P., 2011, Late Triassic porphyritic intrusions and associated volcanic rocks from the Shangri-La region, Yidun terrane, eastern Tibetan Plateau: Adakitic magmatism and porphyry copper mineralization: Lithos, v. 127, p. 24–38.

Wang, E., and Burchfiel, B.C., 2000, Late Cenozoic to Holocene deformation in southwestern Sichuan and adjacent Yunnan, China, and its role in formation of the southeastern part of the Tibetan Plateau: Geological Society of America Bulletin, v. 112, p. 413–423.

Wang, E., Kirby, E., Furlong, K.P., Soest, M.V., Xu, G., Shi, X., Kamp, P.J.J., and Hodges, K.V., 2012, Two-phase growth of high topography in eastern Tibet during the Cenozoic: Nature Geoscience, v. 5, p. 640–645.

Wang, S.X., 2008, Ore geochemistry of the Pulang porphyry copper deposit, Yunnan Province: Unpublished Ph.D thesis, Guiyang, China, University of Chinese Academy of Sciences, 134 p. (in Chinese).

Wang, S.X., Zhang, X.C., Leng, C.B., Qin, C.J., Ma, D.Y., and Wang, W.Q., 2008, Zircon SHRIMP U-Pb dating of the Pulang porphyry copper deposit, northwest Yunnan, China: The ore-forming time limitation and geological significance: Acta Petrologica Sinica, v. 24, p. 2313–2321 (in Chinese with English abs.).

Wang, X.S., Hu, R.Z., Bi, X.W., Leng, C.B., Pan, L.C., Zhu, J.J., and Chen, Y.W., 2014, Petrogenesis of Late Cretaceous I-type granites in the southern Yidun terrane: New constraints on the Late Mesozoic tectonic evolution of the eastern Tibetan Plateau: Lithos, v. 208–209, p. 202–219.

Wiedenbeck, M., Alle, P., Corfu, F., Griffin, W.L., Meier, M., Oberli, F., von Quadt, A., Roddick, J.C., and Speigel, W., 1995, Three natural zircon standards for U-Th-Pb, Lu-Hf, trace element and REE analyses: Geostandards Newsletter, v. 19, p. 1–23.

Wilkinson, B.H., and Kesler, S.E., 2007, Tectonism and exhumation in convergent margin orogens: Insights from ore deposits: Journal of Geology, v. 115, p. 611–627.

Wolf, R.A., Farley, K.A., and Silver, L.T., 1996, Helium diffusion and low-temperature thermochronometry of apatite: Geochimica et Cosmochimica Acta, v. 60, p. 4231–4240.

Wolf, R.A., Farley, K.A., and Kass, D.M., 1998, Modeling of the temperature sensitivity of the apatite (U-Th)/He thermochronometer: Chemical Geology, v. 148, p. 105–114.

Xu, J.F., McInnes, B.I.A., Evans, N.J., and Griffin, W.L., 2006, Emplacement, uplift, and exhumation histories of Tibetan porphyry Cu-Mo-Au deposits: Geochimica et Cosmochimica Acta, v. 70, p. A713-A713.

Yan, D., Zhou, M., Wei, G., Liu, H., Dong, T., Zhang, W., and Jin, Z., 2008, Collapse of Songpan-Garzê orogenic belt resulted from Mesozoic middle-crustal ductile channel flow: Evidences from deformation and metamorphism within Sinian-Paleozoic strata in hinterland of Longmenshan foreland thrust belt: Earth Science Frontiers, v. 15, p. 186–198.

Yang, T.N., Hou, Z Q., Wang, Y., Zhang, H.R., and Wang, Z.L., 2012, Late Paleozoic to Early Mesozoic tectonic evolution of northeast Tibet: Evidence from the Triassic composite western Jinsha-Garze-Litang suture: Tectonics, v. 31, TC4004, doi: 10.1029/ 2011TC003044.

Yanites, B.J., and Kesler, S.E., 2015, A climate signal in exhumation patterns revealed by porphyry copper deposits: Nature Geoscience, v. 8, p. 462–465.

Zeng, P.S., Li, W.C., Wang, H.P., and Li, H., 2006, The Indosinian Pulang superlarge porphyry copper deposit in Yunnan, China: Petrology and chronology: Acta Petrologica Sinica, v. 22, p. 989–1000 (in Chinese with English abs.).

Zeng, Q., Evans, N.J., Mcinnes, B.I.A., Batt, G.E., Mccuaig, C.T., Bagas, L., and Tohver, E., 2013, Geological and thermochronological studies of the Dashui gold deposit, West Qinling orogen, central China: Mineralium Deposita, v. 48, p. 397–412.

Zhang, Y.Z., Replumaz, A., Wang, G.C., Leloup, P.H., Gautheron, C., Bernet, M., van der Beek, P., Paquette, J.L., Wang, A., Zhang, K.X., Chevalier, M.L., and Li, H.B., 2015, Timing and rate of exhumation along the Litang fault system, implication for fault reorganization in southeast Tibet: Tectonics, v. 34, doi: 10.1002/2014TC003671.

Zhang, Y.Z., Replumaz, A., Leloup, P.H., Wang, G.C., Bernet, M., van der Beek, P., Paquette, J.L., and Chevalier, M.L., 2017, Cooling history of the Gongga batholith: Implications for the Xianshuihe fault and Miocene kinematics of SE Tibet: Earth and Planetary Science Letters, v. 465, p. 1–15.

Zhao, J., Qin, K., Li, G., Cao, M., Evans, N.J., Mcinnes, B.I.A., Li, J., Xiao, B., and Chen, L., 2015, The exhumation history of collision-related mineralizing systems in Tibet: Insights from thermal studies of the Sharang and Yaguila deposits, central Lhasa: Ore Geology Reviews, v. 65, p. 1043–1061.

Zhao, J., Qin, K., Xiao, B., McInnes, B., Li, G., Evans, N., Cao, M., and Li, J., 2016, Thermal history of the giant Qulong Cu-Mo deposit, Gangdese metallogenic belt, Tibet: Constraints on magmatic-hydrothermal evolution and exhumation: Gondwana Research, v. 36, p. 390–409.

Cheng-Biao Leng received his B.Sc. degree in geology from Chang'an University, Xi'an, China, in 2005. He completed his Ph.D. degree in economic geology from the University of Chinese Academy of Sciences in 2010. He did three years of post-doctoral research at the Institute of Geology, Chinese Academy of Geological Sciences, from 2013 to 2016. He is now an associate professor at the Institute of Geochemistry, Chinese Academy of Sciences. His research focuses on the formation and preservation of porphyry Cu-Mo-Au deposits.